Thermoablative resistance of ZrB2-SiC-WC ceramics at 2400 °C

Zou, Ji; Rubio Diaz, Virtudes; Binner, Jon G. P.

DOI:
10.1016/j.actamat.2017.05.033

Document Version
Peer reviewed version

Citation for published version (Harvard):
Zou, J, Rubio Diaz, V & Binner, JGP 2017, 'Thermoablative resistance of ZrB_2-SiC-WC ceramics at 2400 °C', *Acta Materialia*, vol. 133, pp. 293-302. https://doi.org/10.1016/j.actamat.2017.05.033

Accepted Manuscript

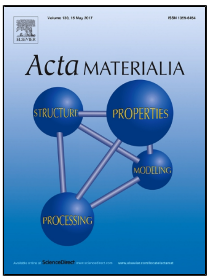

Thermoablative Resistance of ZrB_2-SiC-WC Ceramics at 2400^{o}C

Ji Zou, Virtudes Rubio, Jon Binner

PII:	S1359-6454(17)30420-2
DOI:	10.1016/j.actamat.2017.05.033
Reference:	AM 13794
To appear in:	*Acta Materialia*
Received Date:	16 February 2017
Revised Date:	08 May 2017
Accepted Date:	17 May 2017

Please cite this article as: Ji Zou, Virtudes Rubio, Jon Binner, Thermoablative Resistance of ZrB_2-SiC-WC Ceramics at 2400^{o}C, *Acta Materialia* (2017), doi: 10.1016/j.actamat.2017.05.033

Thermoablative Resistance of ZrB_2-SiC-WC Ceramics at 2400°C

Ji Zou[a*], Virtudes Rubio[a] and Jon Binner[a]

[a] *School of Metallurgy and Materials, University of Birmingham, B15 2TT, Birmingham, UK.*

*Corresponding author

Ji Zou, email: j.zou@bham.ac.uk; zouji1983@gmail.com.

Tel: +44-(0)7478454102;

Fax: +44 (0)1214143971

Abstract

Although ZrB_2-SiC ceramics have been extensively researched for applications at ultra-high temperatures (>2000°C), it is well known that at these temperatures the SiC oxidises actively yielding a gaseous sub-oxide, SiO, rather than the protective, passive oxide product, SiO_2. This limits the high-temperature range of SiC-bearing ceramics for ultra-high temperature applications. In the present work, the addition of 5 vol% WC has been shown to partially eliminate the active oxidation of SiC in ZrB_2-SiC ceramics, even when exposed to an oxyacetylene flame at 2400°C. In contrast to the porous and fragmentary surface observed with ZrB_2-SiC ceramics tested under the same conditions, a dense oxide surface layer was observed that is believed to have resulted in decreasing pO_2 in the layers beneath. This had the effect of changing the chemistry of the system and hence the composition of the phases produced. Clear evidence of the

presence of SiO_2 was observed, thus indicating that the oxidation of the SiC had been partially passive rather than active. A full volatility diagram for WB at 2400°C was derived, and existing volatility diagrams for ZrB_2 and SiC were extended to the same temperature, in order to develop a theoretical understanding of the ablation mechanism. The significantly improved ablation resistance of ZrB_2-SiC-WC is consequently mainly attributed to a competitor transition from tungsten boride (WB) to metallic tungsten in the oxygen partial pressure range 10^{-8} Pa to 10^{-3} Pa, which retards the occurrence of the active oxidation of the SiC phase.

Keywords: Borides; UHTCs; Oxidation; Microstructure; Self-healing.

1. Introduction

It is well known that the efficiency of a heat engine is governed by the temperature at which it operates; the higher the temperature, the better the engine efficiency expected[1]. Whilst metals are currently used for most engines, there is an increasing desire to move to higher performing materials such as ceramics for engines that will operate under the most demanding conditions, including turbines and scramjets[2]. For example, in order to maximize performance and meet the aerodynamic shape constraints of the next generation of hypersonic vehicles, their leading edges and nose cones have to be designed into sharp profiles where active cooling using coolants is impractical. Consequently, these parts have to meet severe operating conditions, including very high heat loads and temperatures, high ablation forces and attack by atomic oxygen amongst other factors[1,3].

Ultra-high Temperature Ceramics (UHTCs) are a class of materials based on refractory metal diborides and carbides that exhibit excellent structural stability at temperatures exceeding 2000°C. Perhaps the most widely investigated of these materials is zirconium diboride, ZrB_2, containing 20 vol% silicon carbide, SiC. Often known as ZS, these ceramics offer a trade-off between density, oxidation resistance, maximum operating temperature, thermal conductivity and mechanical performance at elevated temperature[4-5].

Many ultra-high temperature applications, however, including hypersonic flight, lead to conditions that promote active oxidation of the SiC phase in ZS ceramics. As for monolithic SiC, gaseous SiO can be formed at temperatures in excess of about 1700°C rather than a protective SiO_2 layer, even in a stationary air atmosphere[6,7]. Under more rigorous conditions, e.g. oxyacetylene torch (OAT) testing at 2200°C, the Si-based phase can be completely removed leaving porous monoclinic ZrO_2 ($mZrO_2$) layers on the surface of the ZS[8-11]. Although work aimed at densifying or stabilizing the porous ZrO_2 layer by incorporating rare earth oxides (e.g. SmO_2)[12] or borides (e.g. LaB_6)[13] into the ceramic matrix during processing have been shown to retard the evaporation of the borosilicate glass phase during ablation, the active oxidation of the SiC beneath this layer has not been avoided[8-13]. This then plays a key role in promoting the degradation of the ceramic[4,5,8]. The present work aims to solve this problem by a new approach of suppressing the active oxidation of SiC during ablation of ZS via additions of WC; the resultant ZrB_2-SiC-WC ceramics develop a dense surface oxidation layer when exposed to an oxyacetylene torch generating a heat flux of approximately 10 WM m^{-2} for 300 s.

This paper presents the results of the work undertaken and offers an explanation of the mechanism underpinning the protection achieved.

2. Experimental

Powder mixtures with two different compositions, viz. ZrB_2 – 20 vol% SiC (ZS) and ZrB_2 – 20 vol% SiC – 5 vol% WC (ZSW), were prepared by mixing ZrB_2 (D_{50} = 2.1 μm, H.C. Starck, grade B, Germany), α-SiC (D_{50} = 0.5 μm, H.C. Starck, grade BF-12, Germany) and WC (D_{50} < 1 μm, Hard Alloy Co., Ltd., Zhuzhou, China) powders in appropriate amounts by wet ball mixing followed by rotatory evaporation. 3Y-ZrO_2 balls with a diameter of 10 mm and acetone were used as the mixing media and solvent, respectively. The two powder mixtures were densified in graphite dies using spark plasma sintering (SPS) to yield bodies with a diameter of 30 mm and a thickness of 12 mm. The conditions used were 1950°C for 7 mins under vacuum and a uniaxial loading of 60 MPa during the heat cycle; the heating rate was 100°C min^{-1}.

Cylinders with diameters of 10 mm were prepared by electrical discharge machining the as-sintered discs. After cleaning successively using deionized water and ethanol, the cylinders were fully dried before being subject to oxyacetylene torch (OAT) testing; the latter facility has been described previously[9]. An oxidizing flame was achieved by using an oxygen : acetylene ratio of 1.35 : 1; the pressure was regulated at 0.083 MPa for both gases whilst the flow rates were 0.8 m^3 h^{-1} for the acetylene and 1.1 m^3 h^{-1} for the oxygen. The samples were held in a water-cooled graphite holder and the distance between the flame tip and the sample was set as 25 mm; this yielded a heat flux of ~10 MW m^{-2}. Details of how the heat flux was obtained have been reported elsewhere[14]. All

OAT tests were undertaken for a fixed ablation time of 300 s since ablation is a dynamic process. The temperature was recorded using a two-colour infrared pyrometer (Raytek GmbH, Berlin, Germany) focused on the centre of the hot face of each sample. Meanwhile, the temperature distribution across the samples was also measured using an infrared thermal imaging camera (Thermovision A40, FLIR Systems AB, Sweden).

The surface and cross section of the as-sintered and each as-ablated specimen were characterised using scanning electron microscopy, SEM (JEOL 7000, Tokyo, Japan) equipped with energy-dispersive spectroscopy (EDS). To resolve the overlapping of the kα line between silicon and zirconium from EDS, wavelength dispersive spectroscopy (WDS) was also used via the same SEM; the latter allowed the light elements such as boron and oxygen to be mapped across the polished cross sections. Detailed microstructures for the ZSW after OAT testing were further characterized using transmission electron microscopy, TEM (JEOL 2100, Tokyo, Japan), also with EDS capability, and operated at 200 keV. TEM thin foils were extracted from key locations in the oxidized layers by an *in situ* lift-out technique using a gallium ion focused ion beam (FIB, Quanta 3D FEG, FEI, Eindhoven, Netherlands). In each case, secondary electron images (SEIs) were collected from the SEM with the sample tilted at 52^{o}. Electron and X-ray diffraction (XRD, Bruker, D8 Advance) were combined to identify the phase assemblage in the oxidized layers in the ZSW. For the XRD measurements, a series of patterns were taken from sections at different depths by dry grinding the ablated surface gently using 1200-grit SiC sandpaper.

3. Results and discussion

3.1 Density, microstructure and phase assemblages before ablation

The measured bulk densities for the two compositions were 5.45 g cm^{-3} and 5.95 g cm^{-3} for ZS and ZSW respectively, which correspond to 98.7% and 99.1% of their theoretical values. The microstructures are shown in figure 1. ZrB_2 grains, which appear grey, may be seen to form a continuous matrix with mean grain sizes of 2.8 μm and 2.5 μm in the ZS and ZSW respectively. The SiC phase appears black and is present in both ceramics as an isolated phase, although some elongated SiC grains form agglomerates in the ZS. As expected, the ZSW revealed the presence of reaction-generated phases that were randomly but well distributed, these include ZrC (labelled 'Z' and appearing light grey) and WB (labelled 'W' and appearing white), figure 1b. The reaction paths of WC in the ZrB_2-SiC system with and without the presence of oxygen have been well documented[15,16]. No obvious porosity was observed in either ceramic in accordance with the density measurements and thus will not have played a part in the resulting ablation performance.

3.2 Temperature response during OAT

Figure 2a shows the temperature / time curves for the thermo-ablative assessment undertaken using the OAT tests. Compared with ZS, it was observed that the ZSW heated faster and achieved a higher maximum temperature, ~2400°C after 100 s. One possible reason is the incorporation of WC into the composition reduced the thermal conductivity compared to the ZS ceramics as a result of enhanced phonon scattering through solid solution and phase boundary in ZSW[17]. An alternative explanation is that

the emissivity of the oxide layer was changed due to the presence of the W; rare-earth species have been shown to alter the emissivity of zirconia-based scales[12]. Whatever the explanation, as may be observed, this resulted in a maximum temperature difference of up to 400°C between the two samples during OAT testing. It should also be noted that at elevated temperatures, the thermal conductivity of these ceramics is mainly dominated by the electron contribution. This means that the thermal conductivities will approach a constant value for both ZS and ZSW, regardless of their composition[18]. This could well explain why, ultimately, both ceramics achieved a similar maximum temperature during OAT testing; ~2400°C for ZSW and 2350°C for ZS.

Figure 2b shows how the flame played across the samples during OAT testing. The oxyacetylene flame is normally constituted by an inner cone and an outer feather; however, in this work most of the feather parts of the flame were blocked by the sample under testing and flowed in radial directions, figure 2b. Since the distance between the sample and nozzle tip was 25 mm, which is 10 mm larger than for previous testing[9], the flame covered the sample fairly uniformly and hence the temperature distribution from centre to edge of each sample was limited to less than 150°C according to measurements made using the thermal camera, as shown in figures 2e and f. Nevertheless, all of the analyses presented here were performed in the central region of the sample surface where the temperature was well defined.

Figures 2 c and d show images of ZS and ZSW samples after 300 s of OAT testing. Extensive damage can be seen for the ZS sample with the oxide film formed cracking and detaching readily from the sample surface and damage being clearly visible on the layer below. The primary location of the flame is also easily identified and numerous

macroscopic bubbles were observed on the ZS surface after ablation, implying large quantities of gas were generated during the test. In contrast, the yellowish coloured oxidation layer for the ZSW was much more adherent. It is worth noting that the chipping of the layer around the edge was not due to detachment but rather a consequence of removing the sample from the holder.

3.3 SEM observation

A representative region on the surface of the ZS after OAT testing is shown in figure 3. The top view, figure 3a, shows that the ablation surface is made up of two primary regions, labelled A1, the outer oxide layer, and A2, the material beneath it. A1 was composed of porous ZrO_2, as illustrated in figure 3f, and it can be seen in figures 3b, and to a lesser extent 3c, how this layer readily detached from A2 beneath it. There were also occasional large voids beneath the layer, figure 3g. A cross-sectional observation of A2 indicated that it consisted of a porous ZrO_2 film on top of a porous ZrB_2 layer, both of which were SiC-depleted, figure 3h. This analysis was confirmed by the WDS elemental mappings on a polished cross section, figure 3e. The outermost layer may be seen to be columnar ZrO_2, figure 3c, the pores between the elongated ZrO_2 grains being clearly visible from the Zr map, figure 3e. During ablation these will have served as channels for the evaporating volatile species from the layers below. Although four successive layers are detected from the maps, only three of them, layers I, III and IV, actually belong to the oxidation scale. Layer II, formed mainly of O and C, is the resin that infiltrated into the gap between layers I and III during mounting. This also highlights how readily layer I (which is synonymous with A1) detaches from layer III (which is synonymous with A2) below it. The WDS analysis also shows that layer III was

15 μm thick and confirms that it was constituted of only Zr, B and O and hence was SiC depleted. Such a layer has been observed before during the oxidation or ablation of ZS ceramics[7,8]. Its formation mechanism is known to be related to the active oxidation of SiC during ablation with this occurring prior to the oxidation of the ZrB_2[19]. Layer IV, at the bottom of the structure in figure 3 is the original, unaffected ZrB_2-SiC matrix.

Whilst the total thickness of the oxidation layer for the ZS was ~150 μm, for the ZSW it was slightly thinner at ~120 μm. The cross section shown in figure 4a once again shows four successive layers with different morphologies. This time the oxide scale consisted of: (I) a dense ZrO_2 layer ~60 μm thick; (II) an ~15 μm thick layer of SiO_2 containing some W and Zr inclusions; (III) an apparently SiC depleted layer ~45 μm thick and (IV) once again, the unaffected matrix. Layer I lacks other elements but is rich in O and Zr suggesting the (expected) presence of ZrO_2. Although the mapping didn't provide a clear indication of whether tungsten was present in this layer, spot analyses did confirm some W atoms had been incorporated into the lattice of ZrO_2, figure 4e. According to the ZrO_2-WO_3 phase diagram[20] the solubility of WO_3 in ZrO_2 reaches 4.5 mol% at a temperature as low as 1250^{o}C, further supporting this assumption. It is also interesting that instead of the porous columnar ZrO_2 grains observed in layer I for the ZS after OAT testing, densely packed, equiaxed ZrO_2 grains were present in the equivalent layer for ZSW, figures 4b, 4c and could also be recognized from their cross section 4d. The explanation is probably the presence of the tungsten, since it has been shown to promote the densification of zirconia scales on the top of ZrB_2 via forming a ZrO_2-WO_3 liquid phase during oxidation[21], which might alter the shape and further accelerate the coarsening of ZrO_2 grains.

Importantly, a thin but continuous SiO_2 layer was observed beneath the ZrO_2 layer, figure 4a. The presence of SiO_2 strongly suggests that active oxidation of the SiC was avoided, this in turn suggests that the underlying material was protected by a diffusion-controlled mechanism during ablation. Elemental mapping also suggested that some W-containing phases were present in this layer, however it was hard to clarify the phase assemblage of the W-rich grains because the distribution of O, W and Si in layer II were highly overlapping, figure 4b. In layer III, the elemental mappings reveal that oxygen has penetrated into this region and formed an interconnected network with Zr. Interestingly, there is no B (as expected) but a low concentration of Si in this layer (4b). Layer III clearly does contain W however, and, qualitatively, in a similar amount and distribution as for the unmodified matrix, layer IV.

3.4 TEM observation

To enhance the understanding of the oxidation mechanisms occurring in the ZSW ceramics during OAT ablation, it was necessary to develop a deeper understanding of the phase assemblages in layers II and III. To achieve this, thin slices were lifted out from these regions using FIB and then analysed using TEM, figure 5. In layer II, W-containing particles measuring from 100 nm to 1 μm in size were observed that were well dispersed in a matrix made of glassy SiO_2, figure 5b and c. Considering the latter first, as indicated above, the presence of the SiO_2 first suggests that passive oxidation exists in this layer; SiO_2 could either be generated by passive oxidation of SiC in layer II or formed from species that transport across the apparent SiC-depleted layer through the active oxidation of SiC in layer III. In terms of its structure, it is considered unsurprising that the silica was amorphous in this layer since its crystallization will have

been restrained by the fast cooling from the maximum of 2400°C at the centre of sample surface to room temperature in just a few minutes. Meanwhile, EDS analysis indicated that the particles in the silica mainly contained W and O, figure 5f, whilst indexing of their diffraction patterns, figure 5d, suggested that they were monoclinic WO_3 (a match was obtained with JCPDF 43-1035). Figures 5b and c also reveal that fine ZrO_2 particles were attached to each WO_3 particle in layer II, the phase contrast in figure 5c suggesting the ZrO_2 grains were highly twinned. Twinning is observed in monoclinic ZrO_2 ($mZrO_2$) that has undergone a martensitic tetragonal / monoclinic phase transformation on cooling[22]. The electron diffraction pattern from the ZrO_2 grains confirmed them as being monoclinic, figure 5e.

Layer III contains an apparent mystery. The Si EDS trace in figure 4b suggests that there was relatively little Si-containing phase present, however a sectional view of the same sample, figure 6a, suggests that amorphous SiO_2 and $mZrO_2$ coexist abundantly as separate phases in this layer. It has to be assumed that the SiO_2 was removed during sample preparation. For figure 4 the sample was sectioned and then polished and so it is assumed that the SiO_2 was removed by pull-out; figure 4a could be interpreted as suggesting that grain pull-out had occurred in this region. More interestingly, however, a combination of EDS and electron diffraction, figures 6c and e, verified that metallic W with a BCC lattice was formed in layer III rather than the oxide that was observed in layer II. The presence of a W- (and also a Cu-) containing phase has been reported before following EDS analysis of the outer oxide scale formed on HfB_2-SiC-WC composites after OAT testing, but the structure and composition of that phase wasn't determined[23]. Recently, Silvestroni et al[24] observed nanosized W inclusions trapped

within ZrO_2 grains in the oxidation scale of ZrB_2-15wt% WSi_2 ceramics after static oxidation at 1650°C. Quantitative analysis of the WDS data showed the existence of traces (<3 wt% combined) of O and Zr in the W grains, figure 6d. Putting all of the data together suggests that layer III is composed of crystalized W (see figure 6e), amorphous SiO_2 (see figure 6f) and mZrO_2 (see figure 6g).

3.5 Construction of the volatility phase diagram of WB and SiC

As indicated earlier, the presence of a SiO_2-rich layer below the dense, top ZrO_2 layer in the ZSW after ablation suggests that the latter has protected the SiC from active oxidation. This, in turn, suggests that an oxygen activity gradient developed across the oxidation scale, i.e. oxygen partial pressure in layer IV was significantly lower than in the layers above it, with layer I having the highest value (atmospheric). If true, this also suggests that the final composition of each layer will have corresponded to the outcome of chemical reactions that were influenced by the local pO_2 during ablation or subsequent cooling. Now the vapour pressure of the predominant gaseous species, as a function of temperature and equilibrium partial pressure of oxygen, pO_2, during a material's oxidation can be depicted by volatility diagrams. Thus combining these diagrams for ZrB_2, WB and SiC during oxidation should allow the composition of the oxidation scale to be interpreted. The volatility diagrams for ZrB_2 and SiC have been complied by Fahrenholtz[25] and Heuer[26] respectively (albeit to lower temperatures than used here, see later), whilst that for alpha WB was established in the present work. Before discussing this further, it is appropriate to summarise how the volatility diagram for WB was created; full details will be provided in a future work.

A list of the species considered in the W-B-O system is shown in Table I; the selection is purely based on the NIST-JANAF Thermochemical Tables, to avoid any subjective factors. The relationship between the equilibrium partial pressures of oxygen (pO_2) and B_2O_3 (pB_2O_3) for the oxidation reaction of WB at 2400°C is outlined below as a demonstration. There are two possible reactions to generate B_2O_3 (l) from the reaction between WB and $O_{2\ (g)}$, viz.:

$WB_{(cr)} + 0.5O_{2\ (g)} \rightarrow 0.5WO_{3\ (l)} + 0.5B_2O_{3\ (l)}$ Reaction 1

$WB_{(cr)} + 0.75O_{2\ (g)} \rightarrow W_{(cr)} + 0.5B_2O_{3\ (l)}$ Reaction 2

To establish the relationship between pO_2 and pB_2O_3, the expression for the equilibrium constant (K_{eq}) for both reactions has to be known thus the value for K_{eq} was obtained using Eq. 1 from the change in the standard Gibbs' Energy (ΔG_{rxn}^{o}) for the two reactions. The temperature dependence of ΔG_{rxn}^{o} for both reactions was obtained directly from the database, with T being fixed at 2400°C (as for pO_2, both dependencies are known parameters).

$$\Delta G^{0}_{rxn} = -RT \ln K_{eq} \quad (Eq.1)$$

$$K_{eq}(1) = \frac{a(WO_3)^{0.5}\, a(B_2O_3)^{0.5}}{a(WB)\, a(O_2)^{0.5}} = \frac{1}{p(O_2)^{0.5}} \quad (Eq.2)$$

$$K_{eq}(2) = \frac{a(W)\, a(B_2O_3)^{0.5}}{a(WB)\, a(O_2)^{0.75}} = \frac{1}{p(O_2)^{0.75}} \quad (Eq.3)$$

Below the equilibrium pO_2 determined from Eq. 2, the $B_2O_{3(g)}$ phase will have been in equilibrium with $WB_{(cr)}$ whilst between the equilibrium pO_2 values resulting from Eq. 2 and Eq. 3 the $B_2O_{3(g)}$ phase will have been in equilibrium with $W_{(cr)}$. In both cases the pB_2O_3 will have increased with an increase in the partial pressure of the pO_2. The calculations indicated that no solid W- or B-containing phases existed in this system above the equilibrium pO_2 dictated by Eq.3 as a result of both the evaporation of tungsten oxide and the direct vaporization of the $B_2O_{3(l)}$. Hence, pB_2O_3 will have been independent of pO_2 in this range. Thus, at a given temperature (T) the diagram effectively reflects the relationship between pO_2 and pB_2O_3 combined with the condensed phases that existed. The results for the other W- or B-containing gases were explored using a similar approach and they indicate that gases based on the complex tungsten oxides, $W_3O_{8(g)}$, $W_3O_{9(g)}$ and $W_2O_{6(g)}$, start to be seen when the corresponding solid is tungsten and become dominant when no solid exists in the system. The curves for the other gas-solid reactions in W-B-O system were also computed using the same approach and the overall result is shown in figure 7a.

A similar approach has been taken for the volatility diagrams of SiC and ZrB_2. Although these have previously been calculated[25,26], as indicated earlier, they didn't extend to temperatures as high as 2400^{o}C. For this reason, volatility diagrams for αSiC and ZrB_2 at 2400^{o}C were also compiled and are shown in figures 7b and c respectively.

4. Discussion

4.1 Understanding the formation of layered oxide scales during ablation

According to figure 7a, two transitions can be observed for the main condensed oxidation products of WB at different pO_2 values, these occur when WB transforms to W and when W transforms to a situation where there is no condensed phase at all. This situation allows us to divide the volatility diagram of WB into three regimes:

(1) When $pO_2 < 10^{-8}$ Pa the condensed phase is WB and the major gaseous phases belong to B-O species.
(2) When 10^{-8} Pa $< pO_2 < 10^{-3}$ Pa the condensed phase is W and the gaseous phases belong to B-O species with minor W-O species present;
(3) When $pO_2 > 10^{-3}$ Pa no condensed phases exist and the contribution of B-O and W-O species is almost equal in the gaseous phase.

Similarly, for SiC four regimes can be identified from the volatility diagram at 2400°C:

(1) When $pO_2 < 10^{-13}$ Pa the condensed phase is SiC and the major gaseous phases are $SiO_{(g)}$, $CO_{(g)}$ and $Si_{(g)}$;
(2) When 10^{-13} Pa $< pO_2 < 10^{-12}$ Pa the condensed phase is Si and the major gaseous phases are again $SiO_{(g)}$, $CO_{(g)}$ and $Si_{(g)}$;
(3) When 10^{-12} Pa $< pO_2 < 10^{-4}$ Pa no condensed phases exist and the major gaseous phases are $SiO_{(g)}$ and $CO_{(g)}$.
(4) When $pO_2 > 10^{-4}$ Pa the condensed phase is $SiO_{2(l)}$ and the major gaseous phases are $SiO_{(g)}$, $CO_{(g)}$ and $CO_{2(g)}$.

For the ZrB_2, only two regimes were observed from the volatility diagram at 2400°C, figure 7c, viz.:

(1) When $pO_2 < 10^{-8}$ Pa, the condensed phase is ZrB_2 and the gaseous phases are a mixture of $B_{(g)}$, $BO_{(g)}$, $B_2O_{2(g)}$, and, presumably, others.

(2) When $pO_2 > 10^{-8}$ Pa, the condensed phase is ZrO_2 and the major gaseous phases are $B_2O_{3(g)}$, $BO_{(g)}$, $O_{(g)}$ and $B_2O_{2(g)}$.

Things become interesting if the volatility diagrams of ZrB_2, SiC and WB are combined in an attempt to interpret the oxidation scale formation for ZSW ablated at 2400°C. A prerequisite for doing so is the assumption that all the condensed phases have unit activity, i.e. the condensed phases do not interact significantly with each other in terms of either reactions or the formation of significant solid solutions. This assumption is valid between the ZrB_2 and SiC system based on a previous investigations[19]. For the system involving ZrB_2 and WB, apart from forming a solid solution, no reaction has been reported in any of their binary systems, including ZrB_2 – WB, ZrO_2 – WB, ZrO_2 – W and ZrB_2 – W. If the very limited solutions between ZrB_2 – WB and ZrB_2 – W can be neglected, then the assumption is still valid. Difficulties result, however, from the WB – SiC binary system; even though WB and SiC are not believed to react with each other, reactions between their oxides are entirely possible. Fortunately, at 2400°C no W-based oxides exist as a solid phase in the volatility diagram for WB because of their high vapour pressure, i.e. high volatility. In addition, even if W was potentially able to react with Si, their favourable pO_2 ranges in the diagrams are quite different.

Combining the thermodynamically-favourable condensed phases in the ZrB_2-SiC-WB ternary system with the likely variations in pO_2 results in a diagram that can be divided into several regimes, viz.:

(1) $pO_2 < 10^{-13}$ Pa – the condensed phases are SiC, ZrB_2 and WB;

(2) 10^{-13} Pa < pO_2 <10^{-12} Pa – the condensed phases are Si, ZrB_2 and WB;

(3) 10^{-12} Pa < pO_2 < ~10^{-8} Pa – the condensed phases are ZrB_2 and WB;

(4) 10^{-8} Pa < pO_2 < ~10^{-4} Pa – the condensed phases are ZrO_2 and W;

(5) 10^{-4} Pa < pO_2 < ~10^{-3} Pa – the condensed phases are ZrO_2, SiO_2 and W;

(6) $pO_2 > 10^{-3}$ Pa – the condensed phases are ZrO_2 and SiO_2.

Comparison with the layers observed in figure 4a reveals several mismatches between theory and practice, however several factors need considering. These are indicated in table II. The comments in the latter explain some, but not all of the discrepancies. Two in particular remain. Firstly, between 10^{-4} and 10^{-3} Pa for pO_2, WO_3 was observed rather than metallic tungsten, however, the effects of cooling after the OAT tests needs to be taken in to account. A full volatility diagram of WB at various temperatures was therefore compiled, figure 8, and it is apparent that on decreasing the temperature, the thermodynamically favourable regime for $W_{(cr)}$ shifts towards a lower pO_2 range. For example, the upper bound of pO_2 to create W is 10^{-3}Pa at 2400°C but it reduces to 10^{-10} Pa at 1300°C. More importantly, when performing the calculation at 1800°C or below, the volatility diagram shows that in the oxygen rich zone (>10^{-10} Pa at 1300°C), W_xO_y and B_2O_3 appear as the equilibrium condensed phases. Hence, it can be concluded that the re-oxidation of W into WO_3 in layer II would have been thermodynamically favourable during cooling from 2400°C to room temperature after the OAT testing was complete.

Secondly, whilst the volatility diagram predicts two discrete layers between 10^{-13} and 10^{-8} Pa only a single layer was observed. To address this, a series of XRD patterns from

the oxidized surface were collected by carefully grinding the surface to different depths. As shown in figure 9, the peaks associated with W and WB were both observed at the same depth indicating the co-existence of ZrO_2 – WB and ZrO_2 – W layers, although further TEM analysis was required to confirm this. In addition, XRD patterns obtained at a depth of 70 μm, figure 10, clearly verify the existence of W in the surface oxidation layer of the ZSW ceramics, further supporting the electron diffraction results, figure 6e, and the thermodynamic calculations, figure 7.

4.2 Overall mechanism

For the ZS ceramics, no protective SiO_2-based layer was generated on the oxidation scale during the OAT tests due to the very high temperatures and high gas velocities generated. This led to active oxidation of the SiC, which resulted in a porous, columnar ZrO_2 layer that was weakly bonded to the porous SiC-depleted layer adjacent. Combined with the significant formation of $SiO_{(g)}$ and $CO_{(g)}$, this led to the creation of bubbles and micro-cracks in the surface oxidation layer and subsequently significant spallation.

In contrast, when WC was added to the composition, creating ZSW ceramics, the oxidation of the W-containing phases is believed to have formed liquid phases that enhanced the sintering of the top ZrO_2-based layer, yielding a significantly more dense and equiaxed ceramic that reduced the potential for oxygen transport. This, in turn, is believed to have generated an oxygen partial pressure gradient from the bottom to the top of the oxidation scale, so called self-healing structure during ablation. In addition, at 2400^{o}C when the pO_2 was in a range between 10^{-8} Pa and 10^{-3} Pa, a competition

between the active oxidation of SiC and the generation of W from WB occurred, figure 7a, since both were thermodynamically favourable. Based on the experimental observations, the latter occurred rather than the former. As a result, the active oxidation of SiC was partially retarded and the material suffered significantly less damage during testing.

5. Conclusions

Spark plasma sintered ZrB_2-SiC ceramics with and without WC additions have been exposed to oxyacetylene torch testing under a heat flux of approximately 10 MW m^{-2}. After 300 s of ablation, the maximum temperature recorded for the two ceramics was 2350°C and 2400°C for the ZS and ZSW respectively. Although the ablation temperatures were similar, a significant difference was observed in their oxidation scales. For the ZS, the outermost porous ZrO_2 layer had a columnar microstructure, which will have been permeable to gases, and it readily separated from the SiC-depleted, porous ZrB_2 layer below. Clear evidence was observed for active oxidation of the SiC. When 5 vol% of WC was introduced into the ZrB_2-SiC matrix, however, a dense and adherent zirconia scale was formed on the top of the ZSW during ablation. It is believed that this caused a progressive decrease in the pO_2 present as a function of depth into the oxidation scale. The consequence was the formation of a different set of phases. By constructing the volatility diagrams for WB at 2400°C, and extending those for ZrB_2 and SiC to the same temperature, it has been possible to match the predicted and experimental development of the successive oxidation layers. The result suggests very strongly that the critical factor has been the suppression of the active oxidation of SiC. This has resulted in significantly less damage being observed in the ceramic, even

though it spent more time at higher temperatures and saw a (slightly) higher maximum temperature. Thus, it is believed that a) it seems to be possible to partially avoid the active oxidation of SiC, even under conditions of extreme temperature, and b) to use information from volatility diagrams to aid in the design of ceramic compositions, thus reducing the need for extensive empirical research.

Acknowledgements

Dr Ji Zou was supported by a grant from the UK's Engineering and Physical Science Research Council entitled 'Materials Systems for Extreme Environments', XMat, grant number [EP/K008749/2]. The authors also appreciate the contributions from Dr Prabhu Ramanujam and Miss Lorna Scott Cormack from the University of Birmingham for assistance with the oxyacetylene torch testing.

References

[1] N.P. Padture. Advanced structural ceramics in aerospace propulsion, Nat. Mater. 15 (2016) 804-809.

[2] F. Monteverde, R. Savino, Stability of ultra-high-temperature ZrB_2-SiC ceramics under simulated atmospheric re-entry conditions, J. Eur. Ceram. Soc. 27 (2007) 4797-4805.

[3] R.T. Voland, L.D. Huebner, C.R. McClinton, X-43A Hypersonic vehicle technology development, Acta Astronautica 59 (2006) 181-191.

[4] W.G. Fahrenholtz, J.Binner and J. Zou, Synthesis of ultra-refractory transition metal diboride compounds, Journal of Materials Research 31(2016) 2257-2272.

[5] W.G. Fahrenholtz, G.E. Hilmas, Ultra-high temperature ceramics: Materials for extreme environments, Scripta Mater. 129 (2017) 94-99.

[6] N. Jacobson, B. Harder and D. Myers. Oxidation Transitions for SiC Part I. Active-to-

Passive Transitions, J. Am. Ceram. Soc. 96(2013)838-844.

[7] W. B. Han, P. Hu, X. H. Zhang, J. C. Han, and S. H. Meng, High temperature oxidation at 1900oC of ZrB_2-xSiC ultrahigh-temperature ceramic composites, J. Am. Ceram. Soc. 91(2008) 3328-3334.

[8] J.C. Han, P. Hu, X.H. Zhang, S.H. Meng and W.B. Han, Oxidation-resistant ZrB2–SiC composites at 2200 °C, Composite Science and Technology, 68(2008) 799-806.

[9] A. Paul, S. Venugopal, J.G.P. Binner, B. Vaidhyanathan, A.C.J. Heaton, P.M. Brown, UHTC–carbon fibre composites: Preparation, oxyacetylene torch testing and characterisation, J. Euro. Ceram. Soc. 33(2013)423–432.

[10] Manab Mallik, Ansu. J. Kailath, K.K. Ray and R. Mitra, Effect of SiC content on electrical, thermal and ablative properties of pressureless sintered ZrB_2-based ultrahigh temperature ceramic composites, J. Euro. Ceram. Soc. 37(2017) 559-572.

[11] W.G. Fahrenholtz, G.E. Hilmas, Oxidation of ultra-high temperature transition metal diboride ceramics, International Materials Reviews 57(2012) 61-72.

[12] W. Tanc, M. Adducci, C. Petorak, B. Thompson, A. E. Brenner and R. W. Trice, Effect of rare-earth dopant (Sm) concentration on total hemispherical emissivity and ablation resistance of ZrB_2/SiC coatings, J. Euro. Ceram. Soc. 36(2016) 3833-3841.

[13] X.H. Zhang, P. Hu, J.C. Han, L. Xu and S.H. Meng, The addition of lanthanum hexaboride to zirconium diboride for improved oxidation resistance, Scripta Mater. 57(2007) 1036-1039.

[14] A. Paul, J. G. P. Binner, B. Vaidhyanathan, A. C. J. Heaton and P. M. Brown, Heat flux mapping of oxyacetylene flames and their use to characterise C_f-HfB_2 composites, Advances in Applied Ceramics: Structural, Functional and Bioceramics, 115(2016) 158-165.

[15] J. Zou, G.J. Zhang, Y.M. Kan, Formation of tough interlocking microstructure in ZrB_2-SiC-based ultrahigh-temperature ceramics by pressureless sintering, J. Mater. Res. 24 (2009) 2428-2434.

[16] J. Zou, S.K. Sun, G.J. Zhang, Y.M. Kan, P.L. Wang, T. Ohji, Chemical reactions, anisotropic grain growth and sintering mechanisms of self-reinforced ZrB_2-SiC doped with WC, J. Am. Ceram. Soc. 94 (2011) 1575-1583.

[17] D.L. McClane, W.G. Fahrenholtz, G.E. Hilmas, Thermal properties of (Zr,TM)B_2 solid solutions with TM = Hf, Nb, W, Ti, and Y, J. Am. Ceram. Soc. 97 (2014) 1552-1558.

[18] Hai-Bin Ma, Ji Zou, Jing-Ting Zhu, Ping Lu, Fang-Fang Xu and Guo-Jun Zhang, Thermal and electrical transport in ZrB_2-SiC-WC ceramics up to 1800 °C, Acta Materialia 129(2017) 159-169.

[19] W.G. Fahrenholtz, Thermodynamic Analysis of ZrB_2-SiC Oxidation: Formation of a SiC-Depleted Region, J. Am. Ceram. Soc. 90 (2007) 143-148.

[20] L.Y. Chang, M.G. Scroger and B. Phillips, Condensed Phase Relations in the Systems ZrO_2-WO_2-WO_3 and HfO_2-WO_2-WO_3, J. Am. Ceram. Soc., 1967, 50, 211.

[21] S.C. Zhang, G.E. Hilmas, W.G. Fahrenholtz, Improved oxidation resistance of zirconium diboride by tungsten carbide additions, J. Am. Ceram. Soc. 91 (2008) 3530-3535.

[22] Amanda R. Krause, Hector F. Garces, Gopal Dwivedi, Angel L. Ortiz, Sanjay Sampath, Nitin P. Padture, Calcia-magnesia-alumino-silicate (CMAS)-induced degradation and failure of air plasma sprayed yttria-stabilized zirconia thermal barrier coatings. Acta Materialia 105(2016) 355-366.

[23] C. Carney, A. Paul, S. Venugopal, T. Parthasarathy, J. Binner, A. Katz and P. Brown, Qualitative analysis of hafnium diboride based ultra high temperature ceramics under oxyacetylene torch testing at temperatures above 2100 °C J. Euro. Ceram. Soc. 34(2014) 1045-1051.

[24] Laura Silvestroni, Diletta Sciti, Frederic Monteverde, Kerstin Stricker and Hans-Joachim Kleebe, Microstructure evolution of a W-doped ZrB_2 ceramic upon high-temperature oxidation, J. Am. Ceram. Soc. 100 (2017) 1760-1772.

[25] W.G. Fahrenholtz, The ZrB_2 Volatility Diagram, J. Am. Ceram. Soc. 2005, 88, 3509-3512

[26] A. H. Heuer and V.L.K. Lou, Volatility Diagrams for Silica, Silicon Nitride, and Silicon Carbide and Their Application to High Temperature Decomposition and Oxidation, J. Am. Ceram. Soc. 73 (1990) 2789-2803.

Figure and Table Captions

Table I Species for the calculation of the volatility diagram for αWB.

Table II The differences between SEM observation and thermodynamic prediction.

Fig. 1 As polished surfaces for ZS (a) and ZSW (b) ceramics, ZrC and WB phases are labelled as “Z” and “W” in 1b. Scale bars represent 10μm in 1a and b.

Fig. 2 (a) The peak temperatures as a function of ablation durations recorded from the surface of ZS and ZSW cylinders. Inset in Fig.2a shows (b) a side view of the sample during oxyacetylene torch testing; (c) and (d) are the photographic images of the ZS and ZSW cylinders after ablation. The thermal image of ZSW during OAT test was shown in 2f, together with the maximum and minimum temperatures recorded across the whole sample surface (2e).

Fig. 3 SEM images of as torch tested ZS specimen: (a) a general top view, (b) (c) cross section observations with different magnifications. 3d shows a similar area in 3b, but the image was taken after the polishing the sample mounted in the resin. The indictor in 3d confirms that the resin has infiltrated into the gap in the oxidation structure. WDS mappings in the area circled in 3d are present in Fig3. The top and sectional views of the positions (A1 and A2) marked in Fig.3a are displayed in 3f-h, accordingly.

Fig. 4 The cross section of as torch tested ZSW specimen by SEM (Fig.4a) and corresponding elemental mapping (Si, B, O, W and Zr) by WDS (4b). The top and sectional views of layer I are shown in 4c, 4d and 4e, respectively, together with the EDS pattern (4f) collected from 4c. The dash lines in 4a reveal the multiple layered structures present on the oxidation scale of ZSW sample.

Fig. 5 TEM observation of the thin slice prepared by FIB, which was taken from layer II on the oxidation scale of as-ablated ZSW specimen. The exact positions for lifting out of the TEM slices for Fig.5 and 6 were marked in 5a. 5b and 5c show the representative microstructure on the layer II with different magnifications. The electron diffraction (ED, 5d, 5e) and corresponding EDS patterns (5f, 5g) were collecting from WO_3 and mZrO_2 grains displayed in Fig.5c. '*B*' in 5d and 5e shows the zone axis for performing the electron diffraction (ED) while the dashed rhomboid and its mirror reflections in 5e indicating a twin structure existing in most of the mZrO_2 grain. The ED of amorphous SiO_2 in this layer was not shown, but its pattern resembles the one appeared on Fig.6f.

Fig. 6 SEM/TEM observations on the oxidation scale of as-ablated ZSW specimen, TEM slice was lift out from layer III (a, b). Electron diffraction patterns for W, SiO_2 and ZrO_2, are marked in 6e, 6f and 6g. EDS and WDS of W-containing phase are shown in 6c and 6d, respectively.

Fig. 7 The calculated volatility diagrams for α-tungsten boride (7a), α-silicon carbide (7b) and ZrB_2 (7c) at 2400^{o}C. Unmarked species are gaseous phases.

Fig. 8 The full volatility diagram for tungsten boride calculated at 1300^{o}C, 1800^{o}C and 2200^{o}C.

Fig. 9 XRD of torch tested ZSW samples, patterns were collected from different depths (0, ~40, ~70 and ~120μm) underneath the top of the as-oxidized surface.

Fig.10 A full range of XRD pattern collected from ~70 μm underneath the oxidized surface of ZSW, a series of peaks belong to W with BCC structure could be clearly recognized. Unmarked peaks in figure 10 belong to mZrO_2.

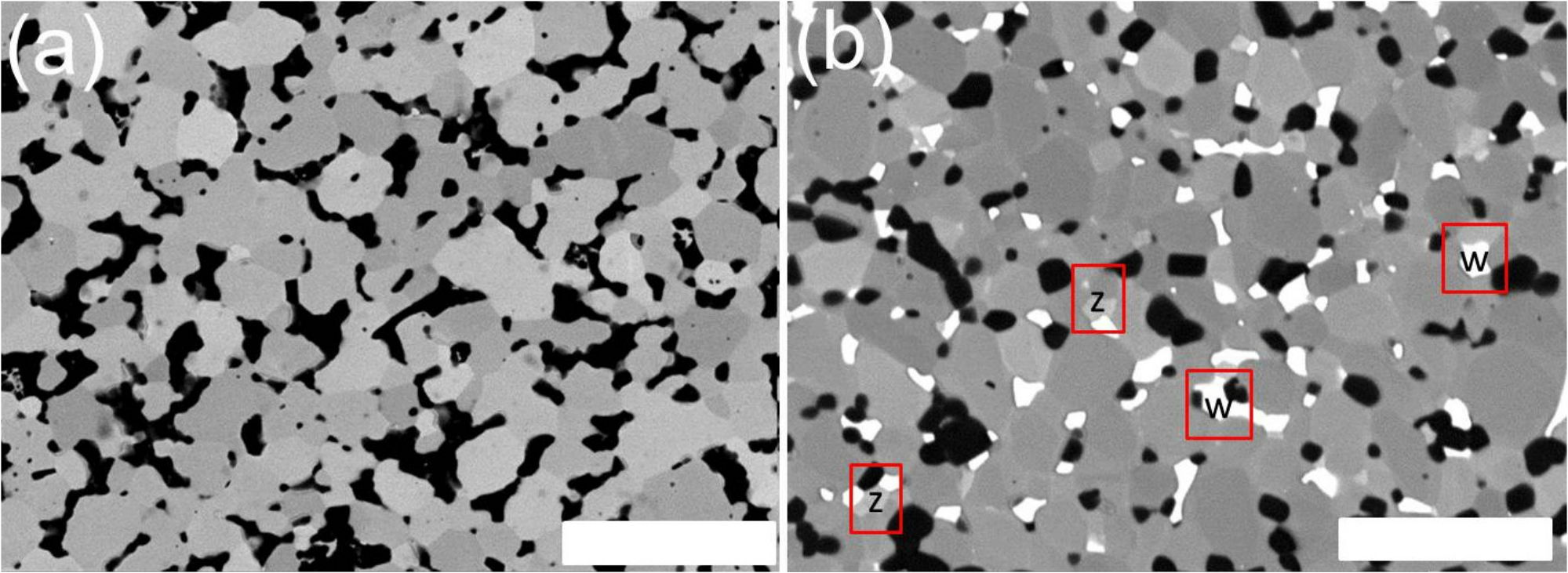
(a)
(b)
Z
W
W
Z

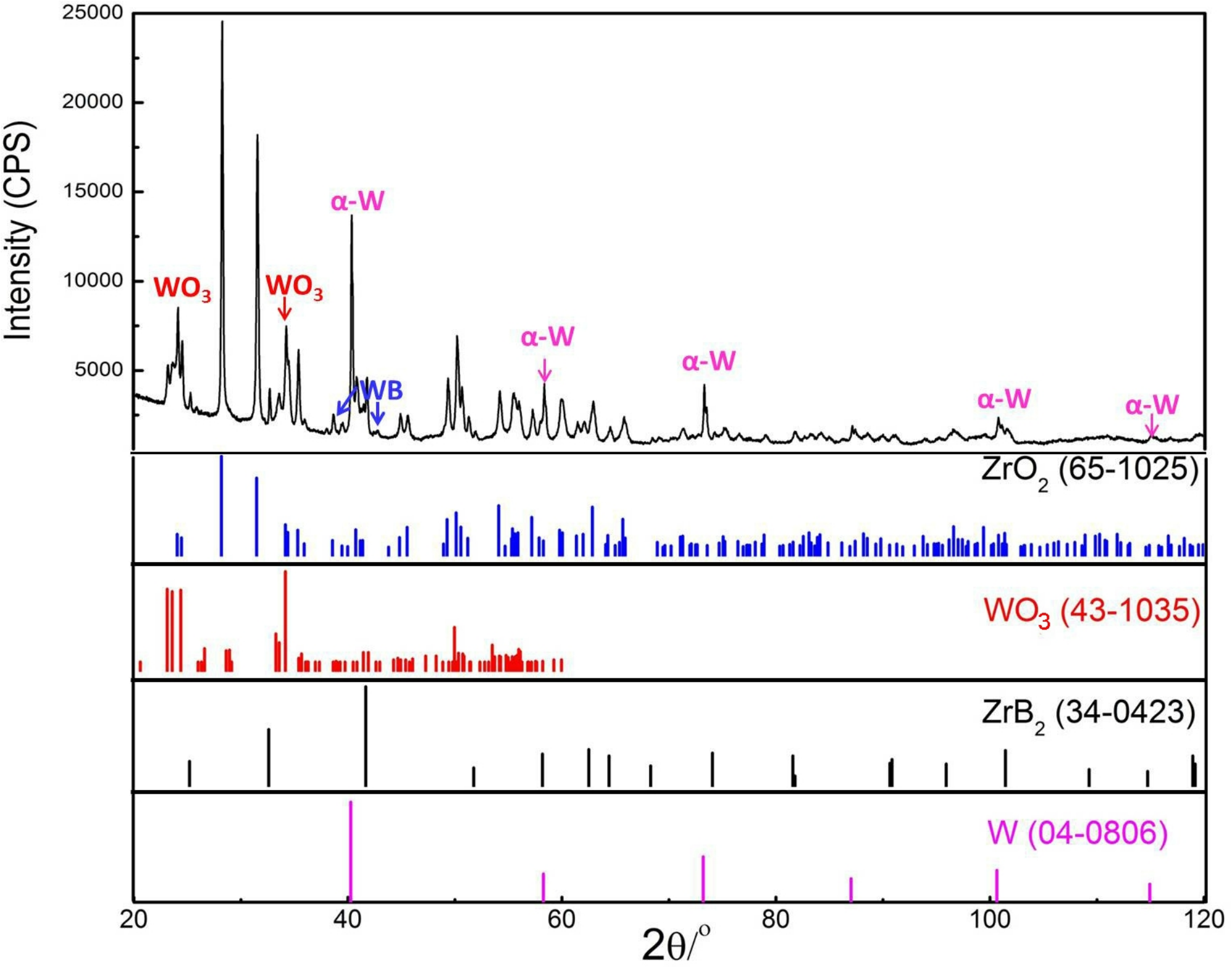
Intensity (CPS)
25000
20000
15000
10000
5000
WO3
WO3
α-W
WB
α-W
α-W
α-W
α-W
ZrO2 (65-1025)
WO3 (43-1035)
ZrB2 (34-0423)
W (04-0806)
20
40
60
80
100
120
2θ/°

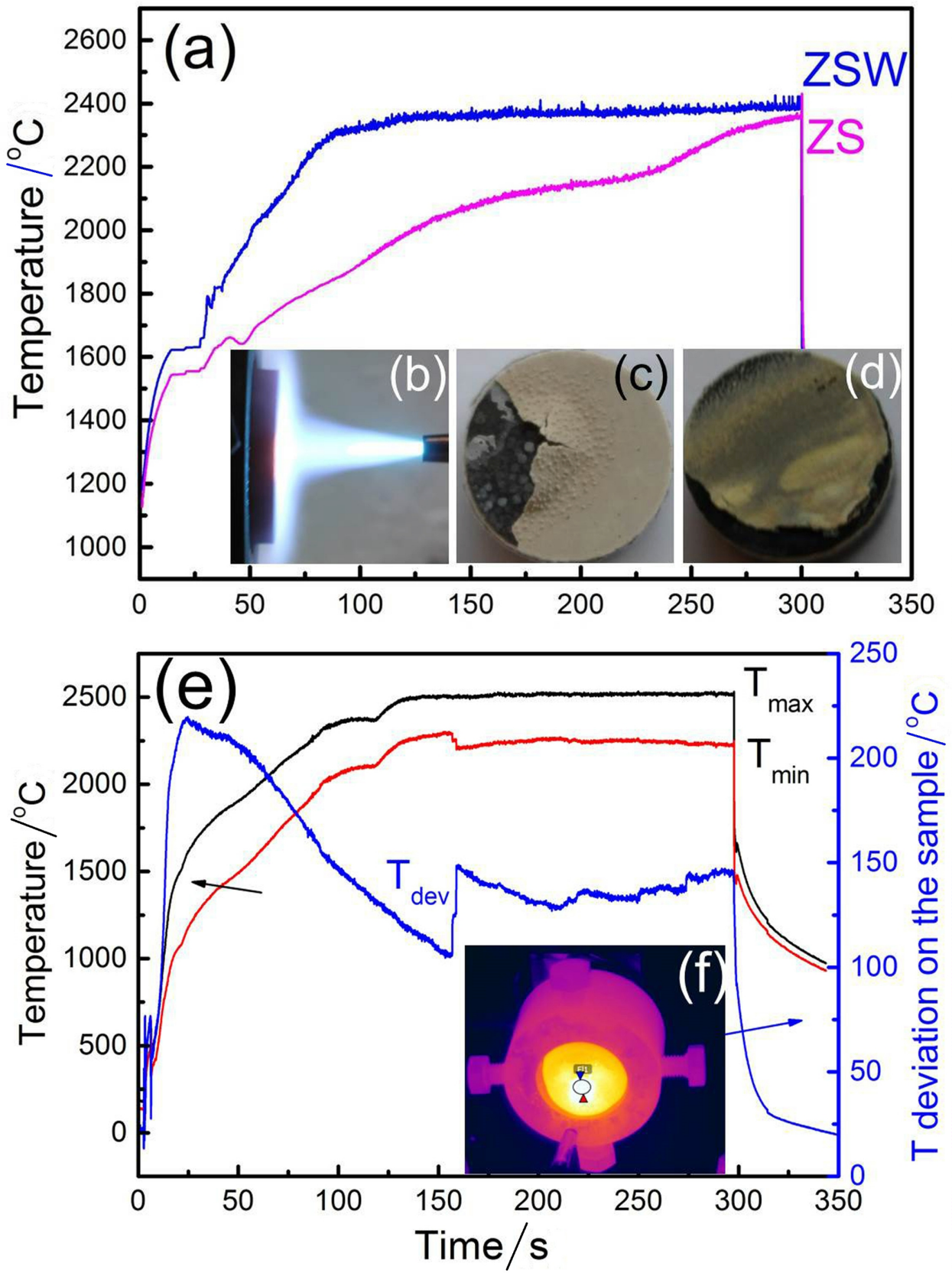
(a)
ZSW
ZS
Temperature /°C
2600
2400
2200
2000
1800
1600
1400
1200
1000
0
50
100
150
200
250
300
350
(b)
(c)
(d)
(e)
T_{max}
T_{min}
T_{dev}
Temperature /°C
2500
2000
1500
1000
500
0
T deviation on the sample /°C
250
200
150
100
50
0
Time /s
(f)

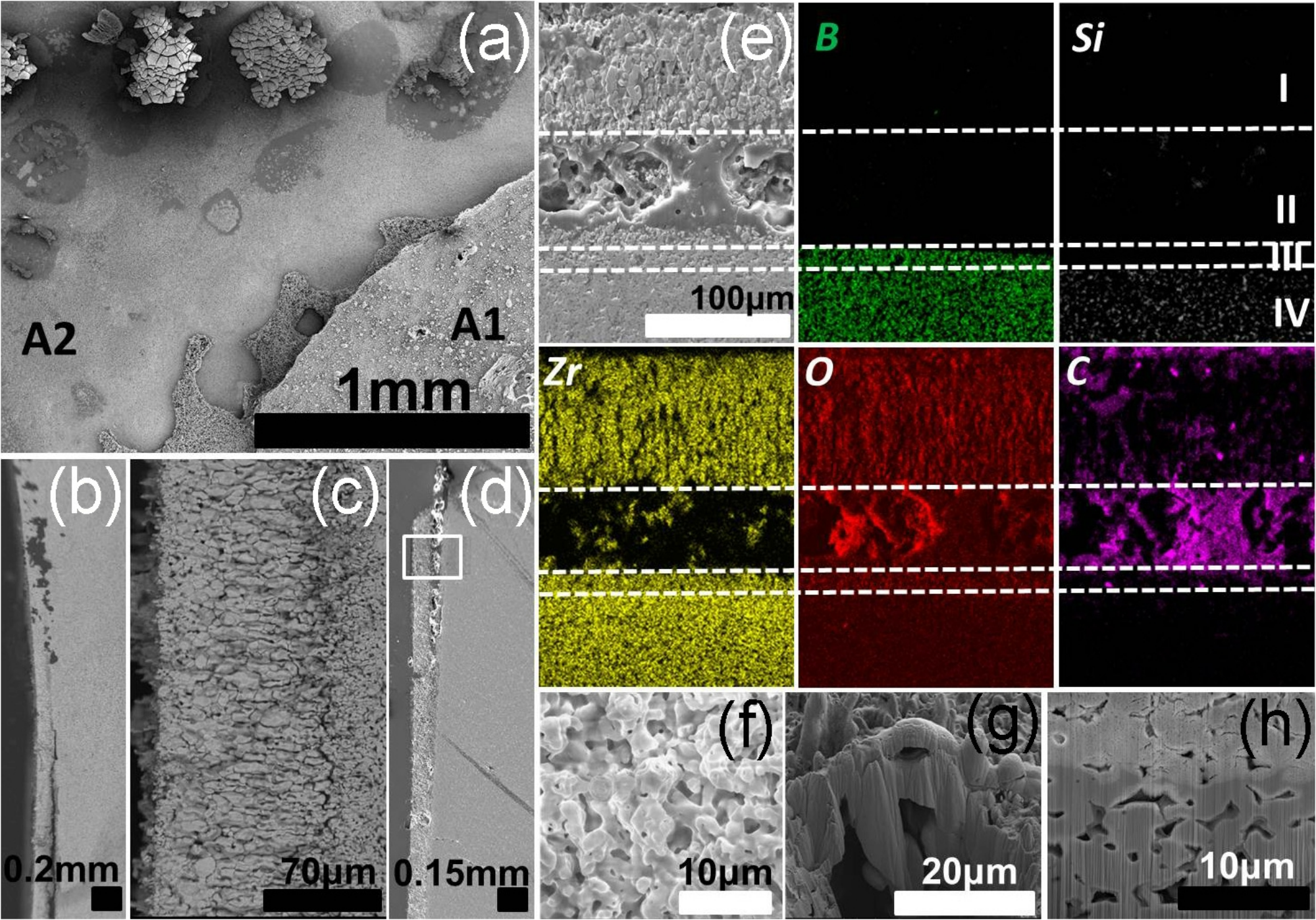
(a)
A2
A1
1mm
(b)
0.2mm
(c)
70μm
(d)
0.15mm
(e)
100μm
B
Si
I
II
III
IV
Zr
O
C
(f)
10μm
(g)
20μm
(h)
10μm

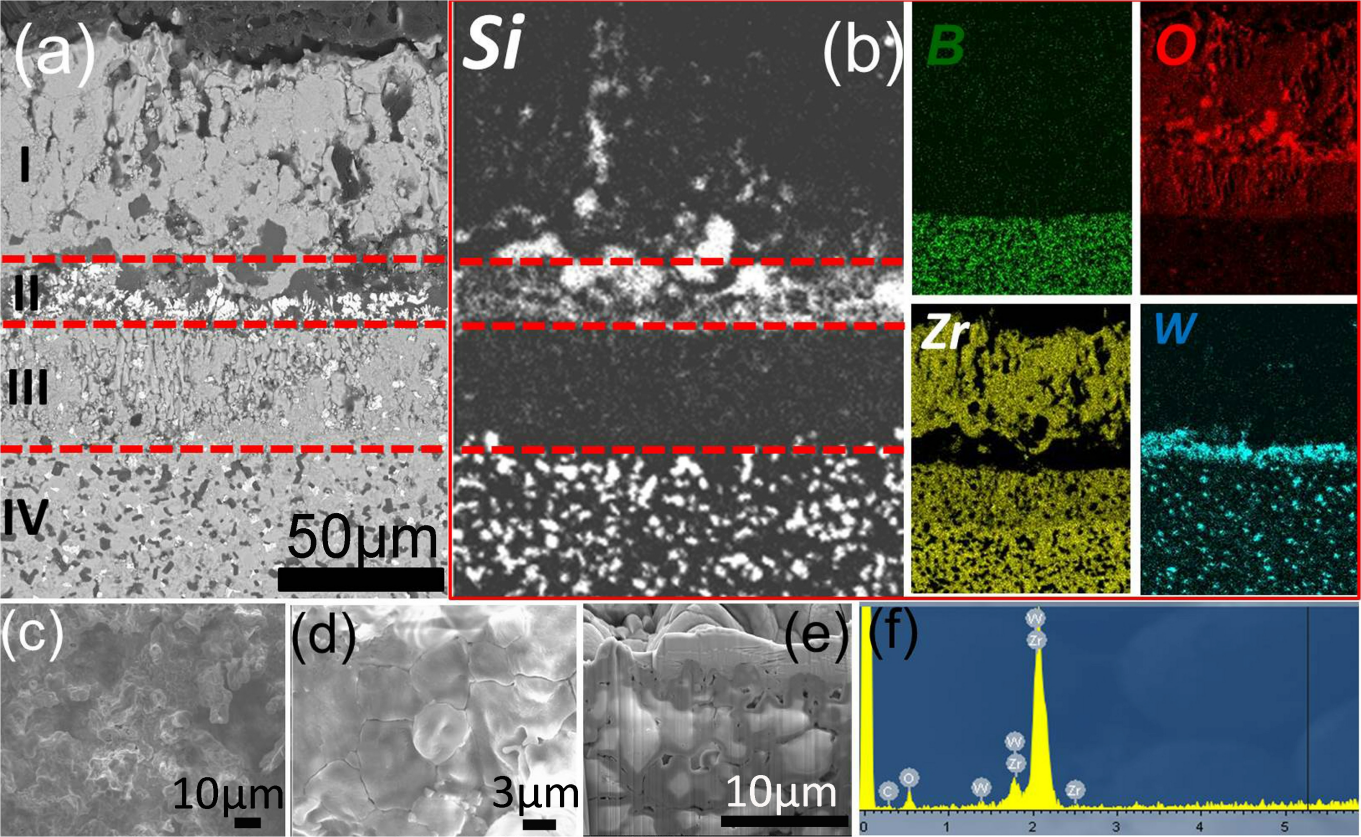
(a)
I
II
III
IV
50μm
Si
(b)
B
O
Zr
W
(c)
10μm
(d)
3μm
(e)
10μm
(f)
W
Zr
O
C
W
W
Zr
Zr
0
1
2
3
4
5

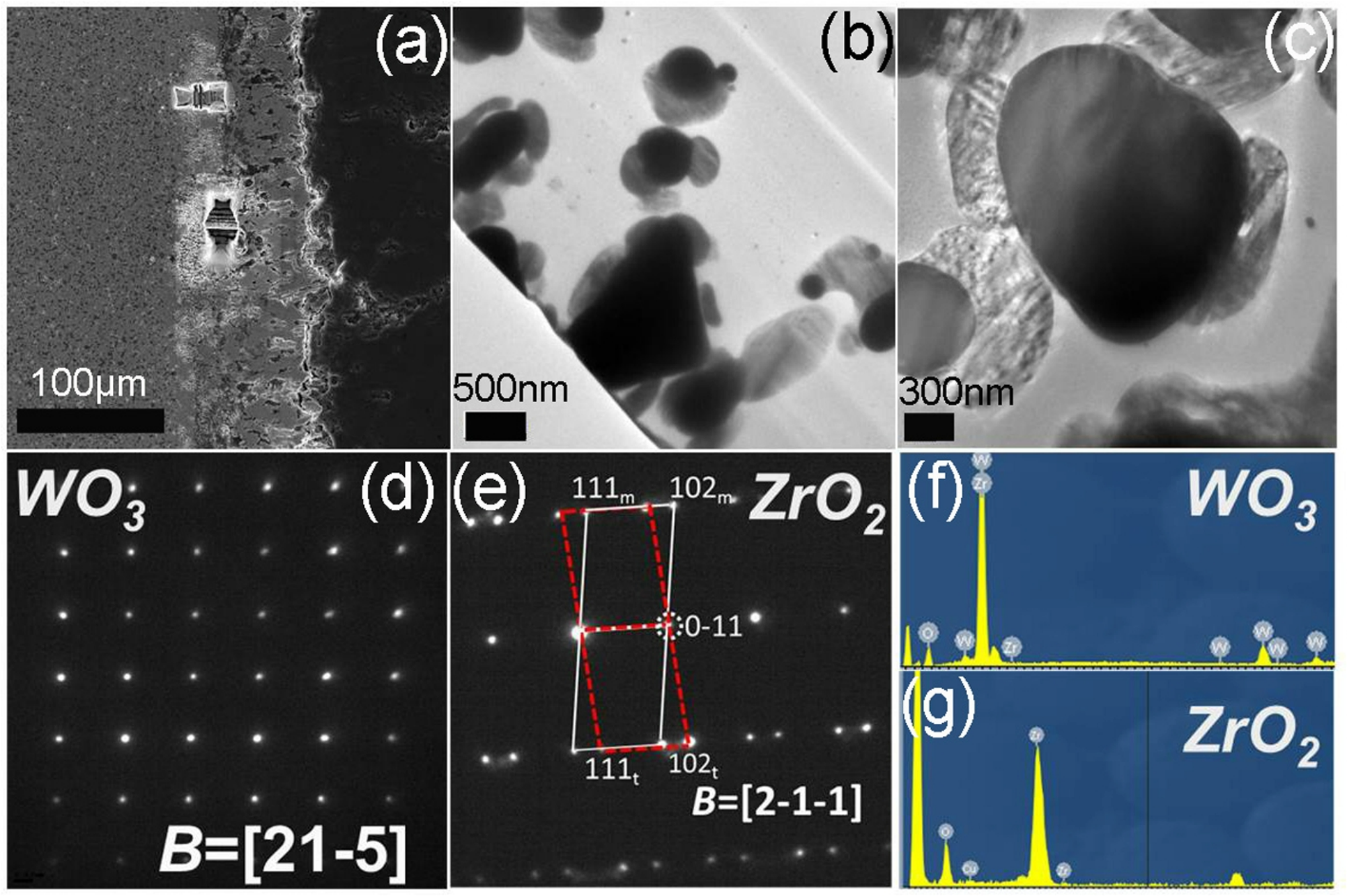
(a)
100μm
(b)
500nm
(c)
300nm
WO3
(d)
B=[21-5]
(e)
111m
102m
ZrO2
0-11
111t
102t
B=[2-1-1]
(f)
WO3
W
Zr
O
(g)
ZrO2
Zr
O
Cu

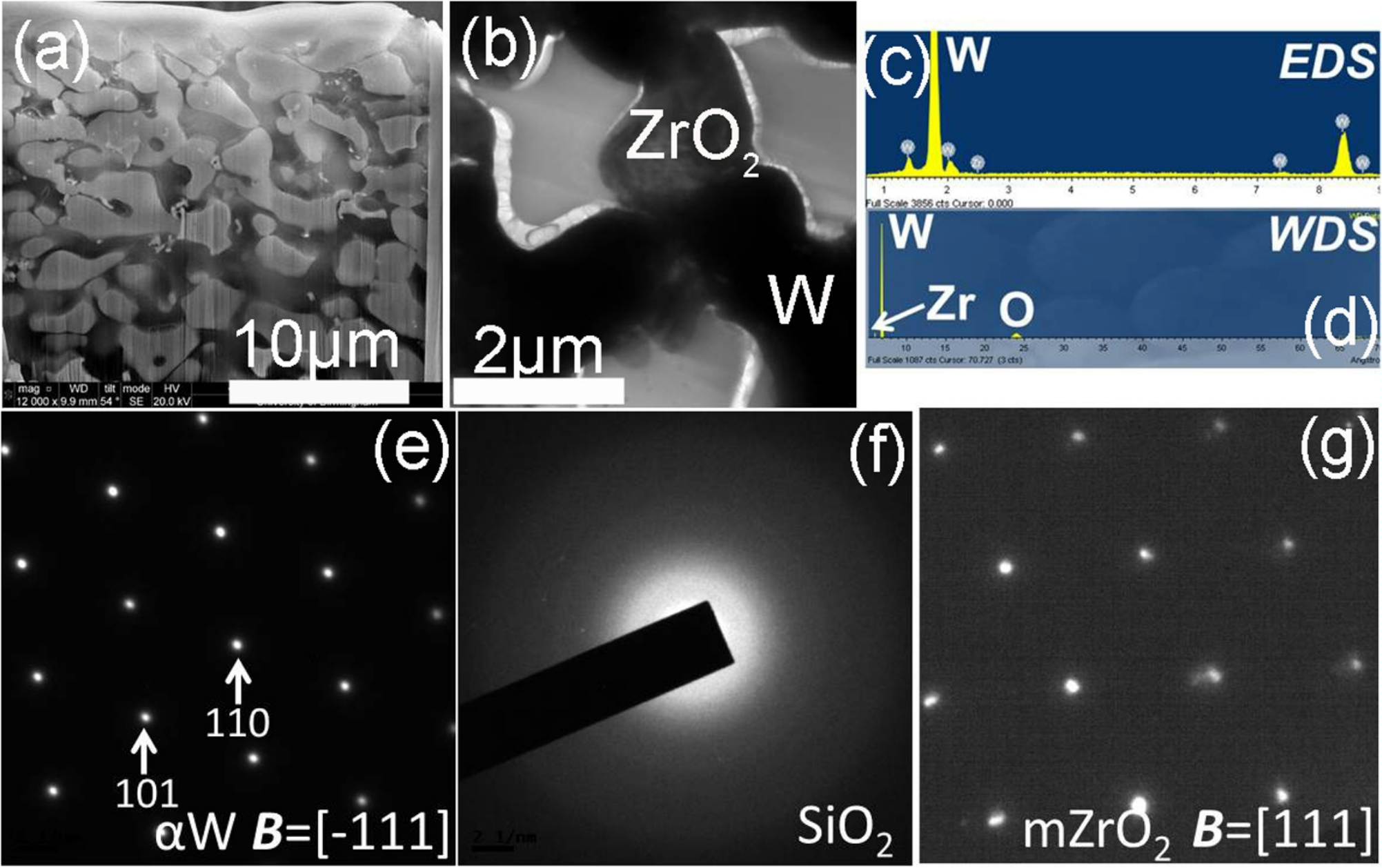
(a)
10μm
mag WD tilt mode HV
12 000 x 9.9 mm 54 ° SE 20.0 kV
(b)
ZrO2
W
2μm
(c)
W
EDS
Full Scale 3856 cts Cursor: 0.000
W
WDS
Zr
O
(d)
Full Scale 1087 cts Cursor: 70.727 (3 cts)
(e)
110
101
αW B=[-111]
(f)
SiO2
(g)
mZrO2 B=[111]

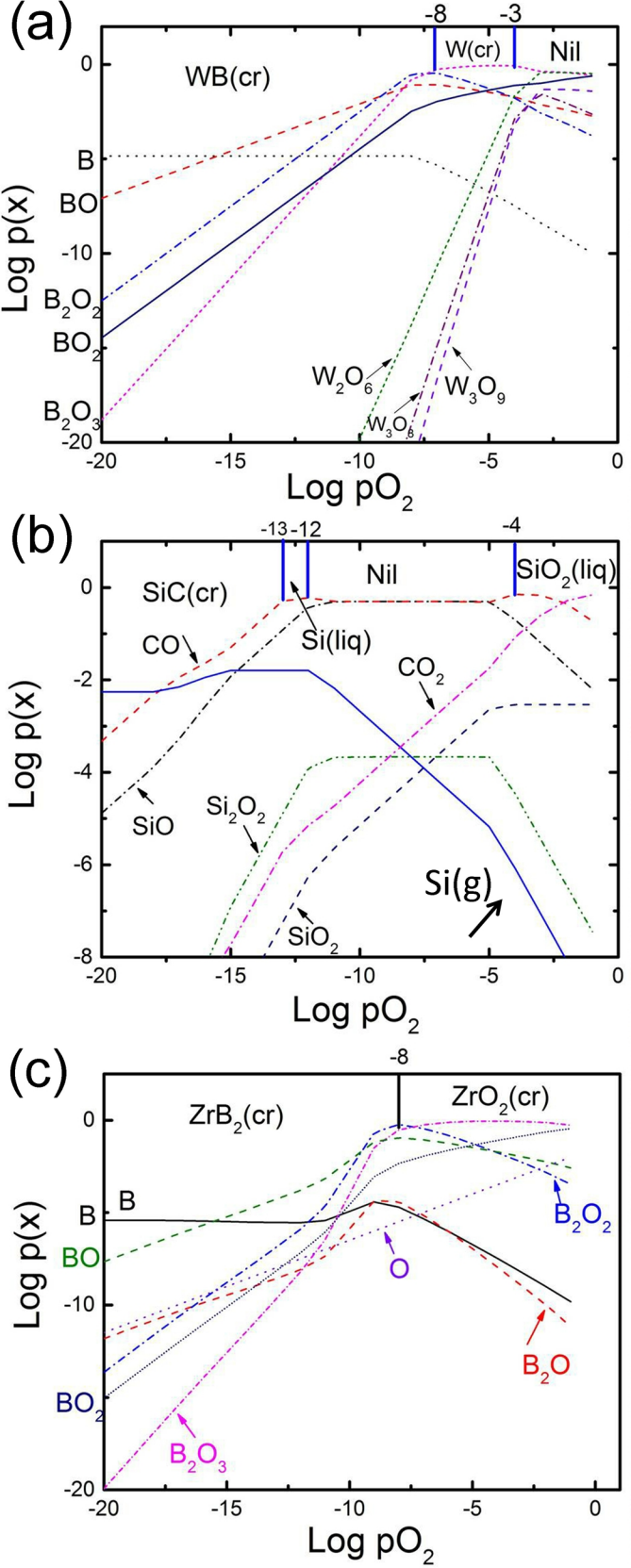
(a)
-8
-3
W(cr)
Nil
WB(cr)
0
B
BO
-10
B_2O_2
BO_2
B_2O_3
-20
W_2O_6
W_3O_9
W_3O_8
Log p(x)
-20
-15
-10
-5
0
Log pO_2
(b)
-13
-12
-4
Nil
SiO_2(liq)
SiC(cr)
CO
Si(liq)
CO_2
SiO
Si_2O_2
Si(g)
SiO_2
0
-2
-4
-6
-8
Log p(x)
-20
-15
-10
-5
0
Log pO_2
(c)
-8
ZrB_2(cr)
ZrO_2(cr)
0
B
B
BO
-10
B_2O_2
O
B_2O
BO_2
B_2O_3
-20
Log p(x)
-20
-15
-10
-5
0
Log pO_2

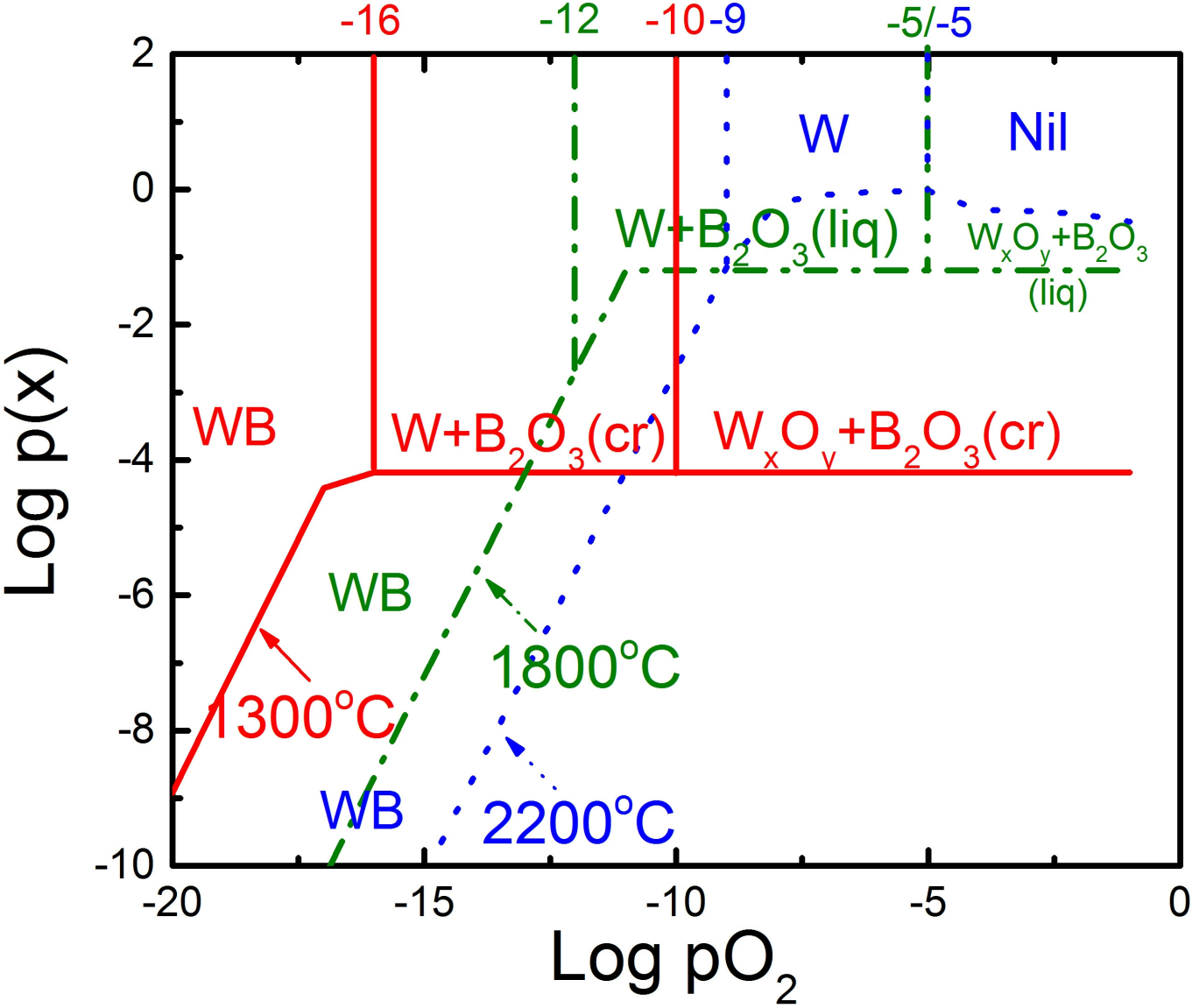
-16
-12
-10
-9
-5/-5
W
Nil
W+B2O3(liq)
WxOy+B2O3
(liq)
WB
W+B2O3(cr)
WxOy+B2O3(cr)
WB
1800°C
1300°C
WB
2200°C
2
0
-2
-4
-6
-8
-10
-20
-15
-10
-5
0
Log p(x)
Log pO2

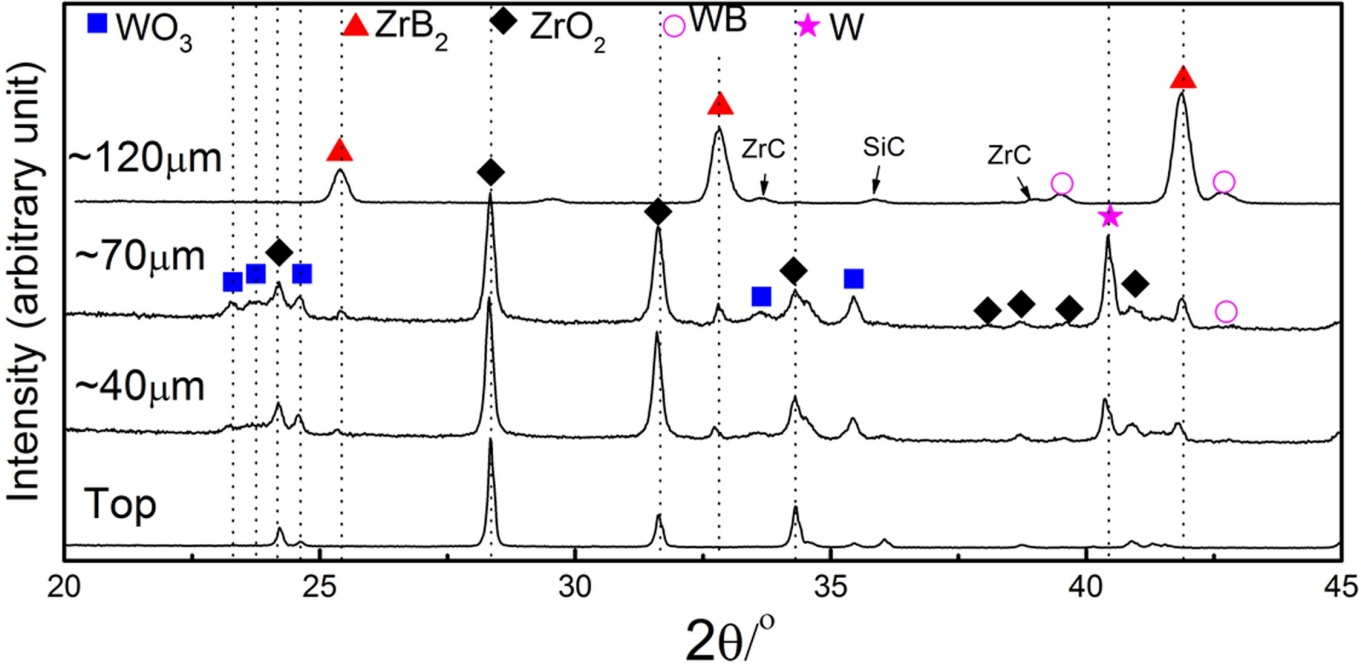
WO3
ZrB2
ZrO2
WB
W
ZrC
SiC
ZrC
~120μm
~70μm
~40μm
Top
Intensity (arbitrary unit)
20
25
30
35
40
45
2θ/°

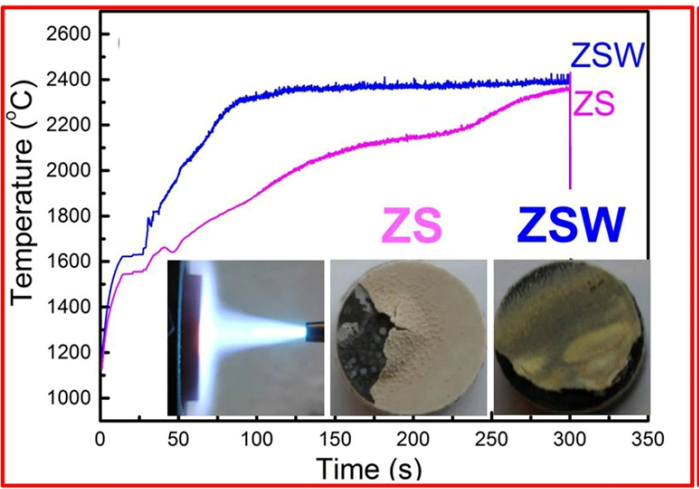

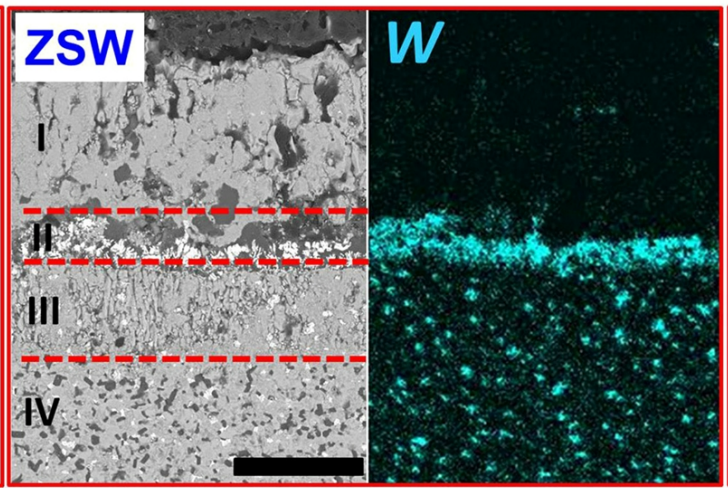

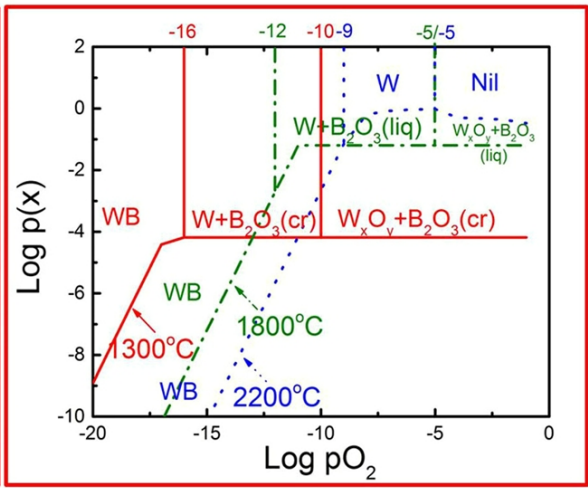

Ablation test at 10MW/m² → **Coherent layer after ablation** ← **First volatility diagram for WB**

↘ ↓ ↙

ZrB_2-SiC-WC (ZSW) ceramics under ablation

Table I Species for the calculation of the volatility diagram for αWB

W species		W-O species		W-B species		B-O species		B species	
gaseous	crystalline	gaseous	crystalline	gaseous	crystalline	gaseous	crystalline	gaseous	crystalline
W	W	W_2O_6 W_3O_9 W_4O_{12} W_5O_{15} WO	W_2O_6 WO_3 WO_2		αWB	BO B_2O_2 B_2O BO_2 O B_2O_3	B_2O_3	B B_2	B

Table II The differences between SEM observation and thermodynamic prediction

pO_2 / Pa	Predicted condensed phases	Comments
$<10^{-13}$	ZrB_2, SiC, WB	The same
$10^{-13} – 10^{-12}$	ZrB_2, Si, WB	Si not observed, but it is in a very narrow pO_2 range
$10^{-12} – 10^{-8}$	ZrO_2, WB	Two layers predicted, only one observed: ZrO_2, SiO_2, W
$10^{-8} – 10^{-4}$	ZrO_2, W	
$10^{-4} – 10^{-3}$	ZrO_2, SiO_2, W	ZrO_2, SiO_2, WO_3 observed in layer II
$>10^{-3}$	ZrO_2, SiO_2	The same, liquid SiO_2 will be removed by ablation